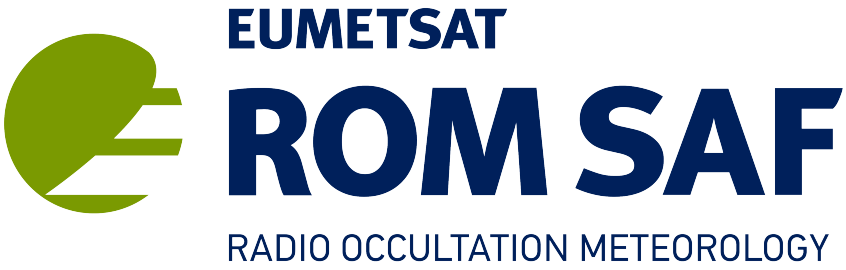

ROM SAF CDOP-3

Visiting Scientist Report 39:

Ionospheric 1D-Var Retrieval Assessment

Sean Elvidge

ROM SAF Consortium
Danish Meteorological Institute (DMI)
European Centre for Medium-Range Weather Forecasts (ECMWF)
Institut d'Estudis Espacials de Catalunya (IEEC)
Met Office (UKMO)

Ref: SAF/ROM/DMI/REP/VS/39
Version: 1.0
Date: 3 January 2022

DOCUMENT AUTHOR TABLE

	Author(s)	*Function*	*Date*
Prepared by:	Sean Elvidge	ROM SAF Visiting Scientist	03/01/22
Reviewed by (Internal):	Sean Healy	ROM SAF Science Coordinator	03/01/22
Approved by:	Sean Healy	ROM SAF Science Coordinator	03/01/22
Approved by:	Kent B. Lauritsen	ROM SAF Project Manager	03/01/22

DOCUMENT CHANGE RECORD

Version	*Date*	*By*	*Description*
Version 0.1	19 July 2021	SE	Initial release
Version 0.2	01 December 2022	SE	Updated following comments from ROM SAF
Version 1.0	03 January 2022	SE	Final Version

DOCUMENT DISTRIBUTION LIST

This VS report is made available at the ROM SAF website

VS AUTHOR AND DURATION

VS Authors

This VS study was carried out by Dr. Sean Elvidge, Associate Professor at the University of Birmingham, UK; email: s.elvidge@bham.ac.uk

VS Duration

The VS study was performed during January - December 2021 at the University of Birmingham, UK.

ROM SAF

The Radio Occultation Meteorology Satellite Application Facility (ROM SAF) is a decentralised processing centre under EUMETSAT which is responsible for operational processing of radio occultation (RO) data from the Metop and Metop-SG satellites and radio occultation data from other missions. The ROM SAF delivers bending angle, refractivity, temperature, pressure, humidity, and other geophysical variables in near real-time for NWP users, as well as reprocessed Climate Data Records (CDRs) and Interim Climate Data Records (ICDRs) for users requiring a higher degree of homogeneity of the RO data sets. The CDRs and ICDRs are further processed into globally gridded monthly-mean data for use in climate monitoring and climate science applications.

The ROM SAF also maintains the Radio Occultation Processing Package (ROPP) which contains software modules that aid users wishing to process, quality-control and assimilate radio occultation data from any radio occultation mission into NWP and other models.

The ROM SAF Leading Entity is the Danish Meteorological Institute (DMI), with Cooperating Entities: i) European Centre for Medium-Range Weather Forecasts (ECMWF) in Reading, United Kingdom, ii) Institut D'Estudis Espacials de Catalunya (IEEC) in Barcelona, Spain, and iii) Met Office in Exeter, United Kingdom. To get access to our products or to read more about the ROM SAF please go to: `http://www.romsaf.org`.

Intellectual Property Rights

List of Contents

Executive Summary

This visiting scientist project has taken the draft Radio Occultation Processing Package (ROPP) 11.0 FORTRAN code for a 1D-Var bending angle retrieval of the ionospheric profile using Vary-Chap functions, further developed it and statistically analysed the results. The main model developments have included adding additional Vary-Chap layers for the retrieval and the development of a new lightweight peak parameter model to use for initialisation. Additional radio occultation data sources from COSMIC-2, Spire Global and simulated observations from 3D ionospheric models have been developed to test the technique on a range of data.

Comparing the 1D-Var retrieval with the COSMIC-2 profile retrieval using co-located (within 200 km) ionosonde observations with all suitable data from 2020 has demonstrated the skill of this approach. Using three or four Vary-Chap layers in the 1D-Var retrieval shows improved performance compared to COSMIC-2 in terms of percentage error for the F2 peak parameters (NmF2 and hmF2). Furthermore, skill in retrieval (compared to COSMIC-2 profiles) throughout the bottomside (~90 km to 300 km) has been demonstrated. With a single Vary-Chap layer the performance is similar, but this improves by approximately 40% when using four-layers.

1 Introduction

1.1 Contractual background

This report forms part of the Task 2 deliverable of the ROM SAF CDOP-3 Visiting Scientist Proposal No. 39: Ionospheric 1D-Var Retrieval Assessment (ROM_AVS20_02).

The objectives of the VS project are:

- Assess the impact of improved a priori information on the Quality Control (QC) and convergence/computational cost of the 1D-Var. Explain how the ROM SAF would access this a priori information. Suggest improvements for the assumed observation uncertainty model.
- Investigate the retrieval solutions below 200 km, and assess the value the 1D-Var - Abel hybrid approach below 200 km.
- Consider how the electron density solutions at the LEO satellite could be validated.

1.2 Technical background

The radio occultation instrument on EUMETSAT's Metop Second Generation (Metop-SG) will measure up to 500 km above the surface of the Earth, and it will provide information on the ionospheric state. The ROM SAF is developing one-dimensional ionospheric electron density profile retrieval systems for Metop-SG [LHPMMC19] as part of CDOP-3 activities, and these activities are likely to be extended into CDOP-4. One dimensional means that ionospheric retrievals ignore horizontal gradients in the electron density, and this source of error is common to all retrievals discussed below.

A specific issue that complicates the application of standard Abel transform techniques (e.g. [SSRH99]) to EPS-SG is that the measurements stop at 500 km, and therefore they do not reach up to the Metop-SG orbit. [LHPMMC19] have developed two retrievals to overcome this problem. The advanced retrieval approach, known as "AVHIRO", has some similarities with the standard optimal estimation (or 1D-Var) approach [Rod00]. It combines an Abel transform solution in one height interval with an estimation of four "Vary-Chap" model ionosphere parameters, which define the shape of the electron density profile. These retrieved parameters are used to estimate the electron densities above 500 km.

The standard description (e.g. [WHF21]) of a Vary-Chap function (first described in [RNHB07] as a generalization of an α-Chapman profile based on the work by [RG69]) with a height-dependent scale height ($H(h)$) is

$$Ne(h) = N_m \left(\frac{H(h)}{H_m} \right)^{-\frac{1}{2}} \exp\left(\frac{1}{2} \left[1 - u - exp(-u) \right] \right), \tag{1.1}$$

where

$$u = \int_{h_m}^{h} \frac{1}{H(h)}\, dh \tag{1.2}$$

for height h, peak density (NmF2) N_m and the scale height at the the height of peak density (hmF2) H_m.

The estimation of the Vary Chap parameters in AVHIRO is based on minimizing a least squares cost function, with two terms. The first term is the fit to a previous state estimate (rather than a "background" constraint) and the second is the fit to the observations, which are Slant Total Electron Content (STEC) measurements. The STEC is the electron density (Ne) integrated along a straight line path (s) between the GNSS and LEO satellites:

$$STEC \propto \int N_e\, ds, \tag{1.3}$$

and it can be computed from a linear combination of the L1 minus L2 phase delay measurements. STEC is used in most ionospheric applications, including ionospheric data assimilation since it is the most abundant dataset [EA19]. Note that, in contrast, bending angles are generally used in neutral atmosphere assimilation, but, to the best of our knowledge, have yet to be used for ionospheric data assimilation.

The relative contribution of the two terms in the AVHIRO cost function is governed by a scaling parameter, λ, which must implicitly be related to the assumed error statistics. The AVHIRO minimization is performed without a tangent-linear or adjoint and it is slow, and not currently considered suitable for operational processing. It has also been suggested that the tangent-linear for a Vary-Chap profile is problematic because of non-linearity, where small changes in the parameters lead to large changes in the gradient [LHPMMC19]. Improvements in both the efficiency and accuracy of AVHIRO is an ongoing area of ROMSAF research in CDOP-3.

In addition to these activities, the ROM SAF has recently developed a prototype, standalone 1D-Var retrieval code, to retrieve the four Vary-Chap parameters. This follows work by [Cul19] who investigated the Vary-Chap ionosphere in connection with modelling both ionospheric bending angle and STEC measurements. We also note that ROPP already includes a 1D-Var option for neutral applications that uses the L1 and/or L2 bending angles. The ionosphere is modelled as a three parameter Chapman layer. This area of work is primarily focused on improving the ionospheric correction in the neutral atmosphere, rather than ionospheric retrieval, but clearly there is some overlap in these activities.

The 1D-Var approach has a clear theoretical basis, with a straightforward statement of the retrieval problem. It provides useful QC diagnostics that can help identify erroneous retrievals, and a theoretical estimate of the solution error covariance matrix, which can be used to estimate the "information content" of the measurements. Estimating the ionospheric state above 500 km is handled easily within this 1D-Var framework.

Traditionally when assimilating STEC observations an estimate of the Differential Code Biases (DCBs) are required (e.g. [FAJB$^+$11]). DCBs are the systematic errors between two GNSS code observations at the same or different frequencies. The Center for Orbit Determination in Europe (CODE) provides estimates of the DCBs for all active GPS and GLONASS

satellites, as well as estimates for a wide range of GNSS receiver stations [COD21]. Alternatively DCBs are commonly estimated during the assimilation step in many ionospheric models by including them in the state vector (e.g. [Ang08, ESSD17]).

To overcome the challenge of DCB estimation in this work the derivative of STEC with respect to the impact parameter, a, ($\partial STEC/\partial a$), has been assimilated. This is the quantity used in the Abel transforms (see Eqn. 14 from [SSRH99]), and to a good approximation it is the L2 minus L1 bending angles, plus a term including the electron density at the LEO (this is more fully described in the main text).

1.3 Report structure

The document is organized as follows:

- Chapter 2: *Ionospheric Retrieval in the ROPP*. An overview of the 1D-Var retrieval code in the Radio Occultation Processing Package (ROPP) 11.0 including a description of the data assimilation, Vary-Chap model, the observations and some example results.
- Chapter 3: *Model Developments*. Updates to the 1D-Var retrieval made in this project, including the additional Vary-Chap layers, a simple model for estimating the background values and the use of different datasets including COSMIC-2.
- Chapter 4: *Statistical Performance of the 1D-Var Retrieval*. Comparison of the peak parameters and bottomside-profile of the 1D-Var retrieval along with COSMIC-2 retrievals compared to co-located ionosonde observations.
- Chapter 5: *Conclusions and Recommendations*.

1.4 List of Acronyms

1D	One dimensional
AVHIRO	Abel-Vary-Chap Hybrid modeling from topside Incomplete RO data
DCB	Differential Code Bias
GNSS	Global Navigation Satellite System
LEO	Low Earth Orbit
Metop-SG	Metop Second Generation
Ne	Electron Density
NWP	Numerical Weather Prediction
PDF	Probability Distribution Function
QC	Quality Control
RO	Radio Occultation
ROM SAF	Radio Occultation Meteorology (ROM) Satellite Application Facility (SAF)
ROPP	Radio Occultation Proessing Package
STEC	Slant Total Electron Content
UPC	Universitat Politécnica de Catalunya

2 Ionospheric Retrieval in the ROPP

2.1 Introduction

The ROM SAF have recently developed a 1D-Var retrieval code to retrieve the parameters for a multi-layer Vary-Chap model. This will be included as part of the Radio Occultation Processing Package (ROPP) 11.0, which is scheduled for release in early 2022. ROPP is a collection of software modules which aids users wishing to assimilate radio occultation (RO) data into Numerical Weather Prediction (NWP) models. The ROPP software is generic, handling any standard GNSS-LEO RO missions, written in Fortran 90 with the code split into several modules [Con20].

2.2 Data Assimilation Preliminaries

Data assimilation models aim to optimally combine disparate measurements with a background model. A range of assimilation methods have been developed; i.e. weighted least squares (WLS) [Pla50], Kalman filters [Kal60], Optimal Interpolation (OI) [Gan63, Edd67] and variational methods [LDT86]. The background model may, in principle, be empirical or a first principles based. Data assimilation models are not real-time, since there is some delay between the data being retrieved and it being assimilated, but they can work in 'near-real-time' (e.g. [AK06] and [EA19]).

In many systems there are usually fewer observations than the number of unknowns, i.e. the system is mathematically under-determined. The observations which are available are subject to experimental uncertainty, and often the observed characteristic is not the variable that is directly modelled. Therefore an observation operator (H) is used to transform the state space to the observation space, i.e.

$$\boldsymbol{y}_o = H(\mathbf{x}) + \boldsymbol{\varepsilon_0} \tag{2.1}$$

where $\mathbf{y}_o$ is a vector of observations, $\boldsymbol{x}$ the true state and $\boldsymbol{\varepsilon_0}$ the observation error.

It is common to want to estimate the state of a system from some given information; for example, to find the TEC through a particular part of the ionosphere. Ideally, a satellite and receiver would be placed at suitable locations, and the TEC directly measured, albeit with some measurement error. However, in practice, this is not possible and the value has to be estimated. The first approach is to just use data from the nearest satellite/receiver pair to the region of interest. Secondly, if more than one satellite/receiver pair exist, then both can be used to interpolate the information in order to estimate the TEC. This estimation can be improved by using more satellite/receiver data. However, depending on a number of factors, including the distance of the satellite from the point of interest, each new piece of information should be weighted differently depending on how much the data is "trusted". Data assimilation is the art of optimally combining various sources of information to estimate the true state of the system.

The subject of data assimilation is both wide and varied, there are a number of excellent books on the subject which should be consulted for a detailed discussion of the topic, specifically those by [Rod00, Kal03, Eve09].

In a variational retrieval system the estimate of the state vector is obtained using the observations combined with a priori information. Since the observations, and a priori information, are only known up to certain levels of confidence these are usually described using probability distribution functions (PDFs). By assuming these PDFs are Gaussian and the errors are uncorrelated Bayes' theorem can be used to describe this problem as the minimization of a cost function (e.g. [Tal10]):

$$J(\boldsymbol{x}) = \frac{1}{2}(\boldsymbol{x}-\boldsymbol{x}_b)^T \boldsymbol{B}^{-1}(\boldsymbol{x}-\boldsymbol{x}_b) + \frac{1}{2}(\boldsymbol{y}_o - H\boldsymbol{x})^T \boldsymbol{R}^{-1}(\boldsymbol{y}_o - H(\boldsymbol{x})) \tag{2.2}$$

where $\boldsymbol{B}$ is the background error covariance matrix and $\boldsymbol{R}$ the observation error covariance matrix.

2.3 Vary-Chap Background Model

Equation 1.1, gave the Vary-Chap function with a height-dependent scale height $H(h)$. In practice, this height-dependent scale height can be difficult to determine [WHF21, KMB+09, NRHB12]. Throughout this work the scale height used in the Vary-Chap profile is based on a constant reference scale height, H_0 giving:

$$Ne(h) = N_m \left(\frac{H_0}{H_m}\right)^{-\frac{1}{2}} \exp\left(\frac{1}{2}[1 - z - exp(-z)]\right), \tag{2.3}$$

where the scale height at the the height of peak density, H_m is given in terms of k, the vertical gradient of the scale height:

$$H_m = H_0 + k(h - hmF2) \tag{2.4}$$

and then taking the integral of Equation 1.2 gives:

$$z = \frac{1}{k} \cdot \log\left(\left[1 + \frac{k(h - hmF2)}{H_0}\right]\right) \tag{2.5}$$

Using Equations 2.3 to 2.5 the Vary-Chap profile with 'standard' values of

$$\begin{aligned} NmF2 &= 2\times10^{12} \text{ electrons}/m^3 \\ hmF2 &= 300 \text{ km} \\ H_{0,F2} &= 50 \text{ km} \\ k_{F2} &= 0.15 \end{aligned}$$

across an altitude range of 100 km to 600 km is shown in Figure 2.1.

This "one-layer" Vary-Chap profile provides a good approximation to the standard electron density profile. However a better approximation can be formed through the addition of multiple Vary-Chap profiles. In ROPP a second layer Vary-Chap is added with the additional

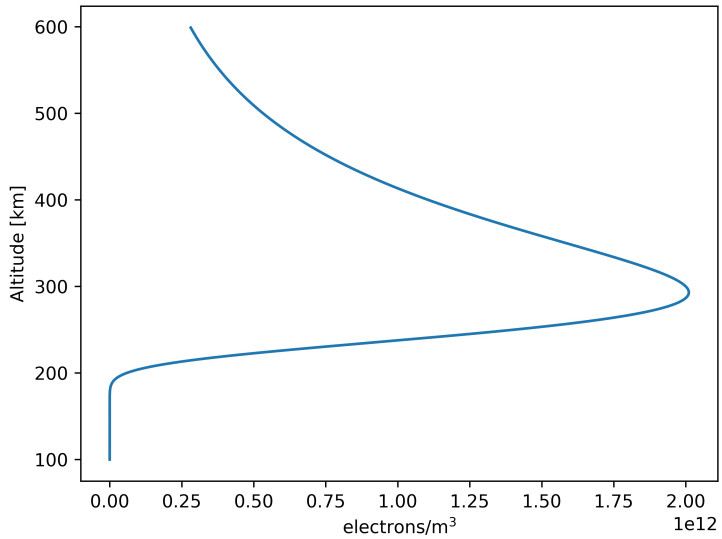

Figure 2.1: *Example of a Vary-Chap profile with* $NmF2 = 2 \times 10^{12}$*,* $hmF2 = 300$*,* $H_0 = 50$ *and* $k = 0.15$*.*

parameters:

$$\begin{aligned} NmF1 &= 5 \times 10^{11} \text{ electrons}/m^3 \\ hmF1 &= 170 \text{ km} \\ H_{0,F1} &= 30 \text{ km} \\ k_{F1} &= 0.05 \end{aligned}$$

The resulting ionospheric profile is shown in Figure 2.2.

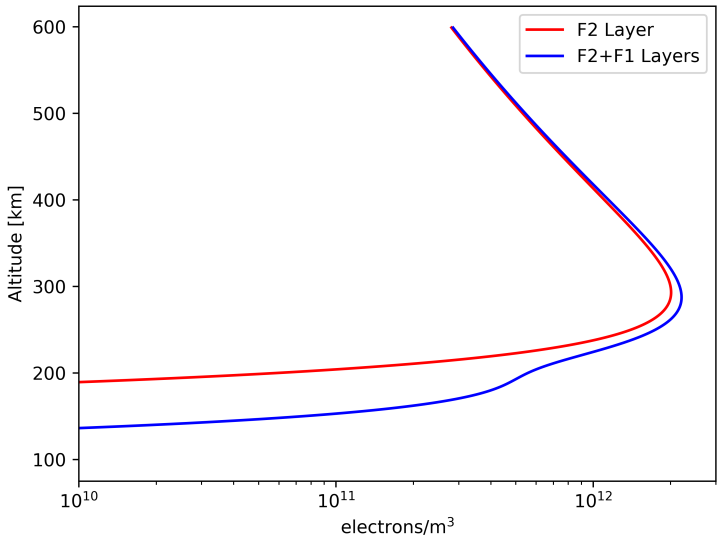

Figure 2.2: *Example of a two-layer Vary-Chap profile.*

2.4 Observations

To overcome the need for estimation of the Differential Code Biases (DCBs) in this work the derivative of STEC with respect to the impact parameter, a, $(\partial STEC/\partial a)$, has been assimilated. This is the quantity used in the Abel transforms (see Eqn. 14 in [SSRH99]), and to a good approximation it is the L2 minus L1 bending angles, plus a term including the electron density at the LEO. This derivative is essentially the RO bending angle which is delivered by the ROM SAF.

The slant TEC ($STEC$) is the column integrated electron density (Ne) along the path ds, $\int Ne\,ds$. To a first approximation the ionospheric phase delay for a frequency i, ϕ_i, is given by

$$\phi_i = -\kappa \frac{STEC}{f_i^2} \tag{2.6}$$

where κ is a proportional constant given by

$$\kappa = \frac{q^2}{8\pi^2 m_e \varepsilon_0} \approx 40.308 \text{ m}^3\text{s}^{-2} \tag{2.7}$$

where q is the electron charge, m_e the electron mass and ε_0 is the vacuum permittivity.

In an RO geometry, assuming that the electron density is only a function of height (spherical symmetry) the STEC between a GNSS satellite at radius r_G and a LEO satellite at radius r_L is given by ([SSRH99])

$$STEC_i = \int_a^{r_L} \frac{rNe(r)}{\sqrt{r^2-a^2}}\,dr + \int_a^{rG} \frac{rNe(r)}{\sqrt{r^2-a^2}}\,dr$$
$$= \left[\int_a^{r_L} + \int_a^{r_G}\right] \frac{rNe(r)}{\sqrt{r^2-a^2}}\,dr \tag{2.8}$$

where a is the impact parameter and $Ne(r)$ is the electron density at radius r. Assuming the electron density at GNSS altitudes is 0 ($Ne(r_G) = 0$), using the substitution $ds = (r/\sqrt{r^2-a^2})\,dr$ and integrating Equation 2.8 by parts gives

$$STEC_i = Ne(r_L)\sqrt{(r_L^2-a^2)} - \left[\int_a^{r_L} + \int_a^{r_G}\right] \sqrt{r^2-a^2}\frac{dNe(r)}{dr}\,dr \tag{2.9}$$

The derivative of Equation 2.9 with respect to the impact parameter, a, gives our required $\partial STEC/\partial a$:

$$\frac{\partial STEC_i}{\partial a} = -\frac{Ne(r_L)a}{\sqrt{(r_L^2-a^2)}} + a\left[\int_a^{r_L} + \int_a^{r_G}\right] \frac{\frac{dNe(r)}{dr}}{\sqrt{r^2-a^2}}\,dr. \tag{2.10}$$

Finally, note that the integral in Equation 2.10 is f_i^2/κ times the standard approximate 1D bending angle at the impact parameter a, α_i:

$$\alpha_i(a) = -2a\int_{r_t}^{\infty} \frac{\frac{dn_i}{dr}}{n_i\sqrt{(n_i r)^2-a^2}}\,dr \tag{2.11}$$

assuming spherical symmetry and where n_i is the refractive index and r_t is the tangent height of the ray path [HC15]. The refractive index is often approximated by

$$n_i \approx 1 + 10^{-6}N_n(r) - \frac{\kappa Ne(r)}{f_i^2}, \tag{2.12}$$

where N_n is the neutral refractivity.

2.5 Example Results

Using example observational data from Universitat Politécnica de Catalunya (UPC), Figure 2.3, and the 1D-Var assimilation code from ROPP gives the assimilation analysis, x_a, plotted in Figure 2.4. The analysis parameters, compared to the background are shown in Table 3.1. Both a one- and two-layer Vary-Chap layers are included. In both cases the F2 layer parameters are very similar, with the peak density an order of magnitude lower in the analysis compared to the background.

Figure 2.4 shows the profiles generated from these parameters as well as, in green, the Abel

Table 2.1: *Background and analysis parameters for the one and two-layer Vary-Chap.*

	Parameters							
	$NmF2$	$hmF2$	$H_{0,F2}$	k_{F2}	$NmF1$	$hmF1$	$H_{0,F1}$	k_{F1}
Background 1-Layer	2×10^{12}	300	50	0.15				
Analysis 1-Layer	1.48×10^{11}	316	47	0.02				
Background 2-Layers	2×10^{12}	300	50	0.15	5×10^{11}	170	30	0.05
Analysis 2-Layers	1.56×10^{11}	316	48	0.06	3.2×10^{10}	156	22	0.36

transform of the observations for comparison [SSRH99]). Clearly the analysis output from the 1D-Var provides a result very close to that of the Abel transform. Structure below 150 km is not present at all in the one-layer Vary-Chap, as expected. The two-layer Vary-Chap provides a very close approximation to the Abel transform, reconstructing the trend of the observations below 150 km.

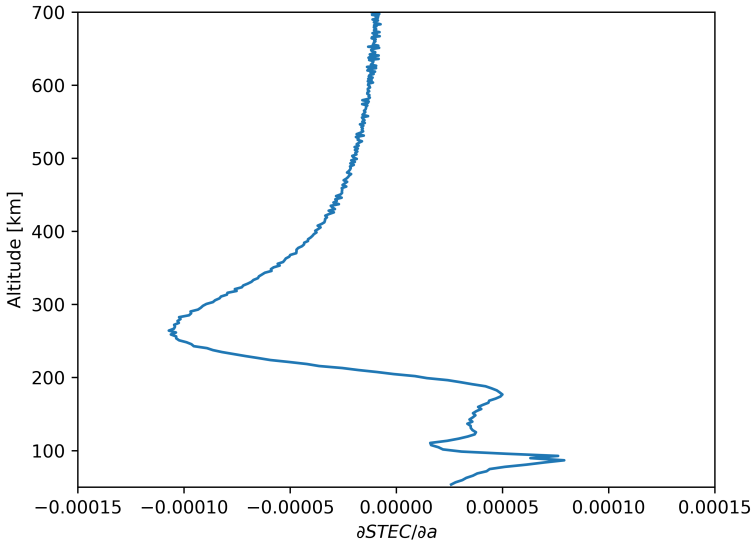

Figure 2.3: *Example $\partial STEC/\partial a$ observation courtesy of UPC.*

Additionally, it is interesting to see how the 1D-Var performs in the observation space, rather than state space. In Figure 2.5 the improvement of both the one- and two-layer Vary-Chap models is clear. However both models underestimate the bending angle values at approximately -1×10^{-4}, the background model actually represents this value very well, but approximately 100 km too high.

The additional structure in the observations below 100 km is likely noise in the observations. Whilst in Figure 2.4 through the Abel transform this suggests the presence of an E-layer, it is not clear how much signal is present at these lower altitudes. For example, Figure 2.6 shows the observations from a different example file, plotted on a log scale to highlight the differences. Here it can be seen that the sub-150 km structure seems much noisier, with no obvious E-region. The amount of signal available in these lower altitudes is further investigated later in this report.

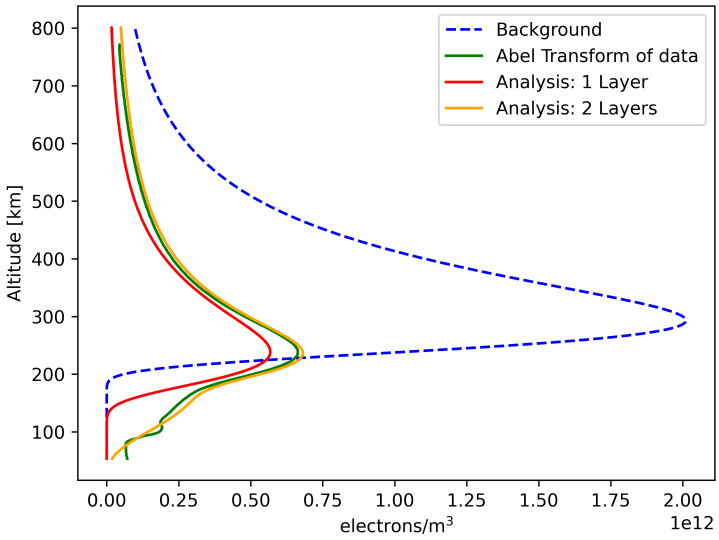

Figure 2.4: *Example post-assimilation results using the data shown in Figure 2.3.*

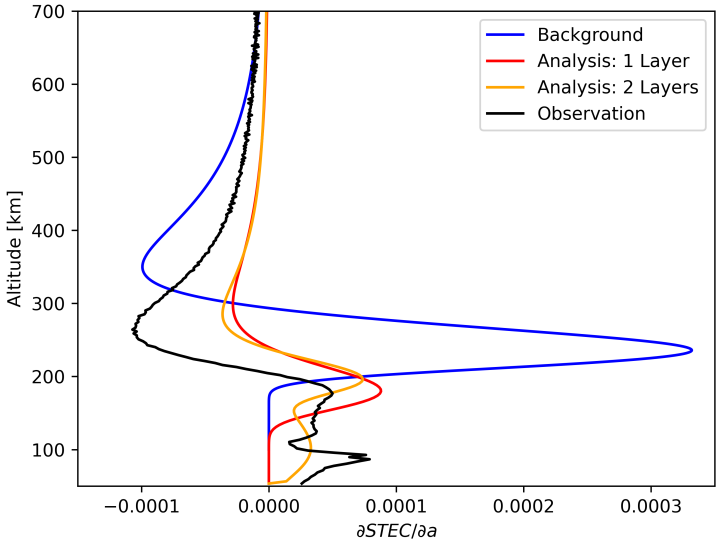

Figure 2.5: *Example post-assimilation results using the data shown in Figure 2.3 in the observation space.*

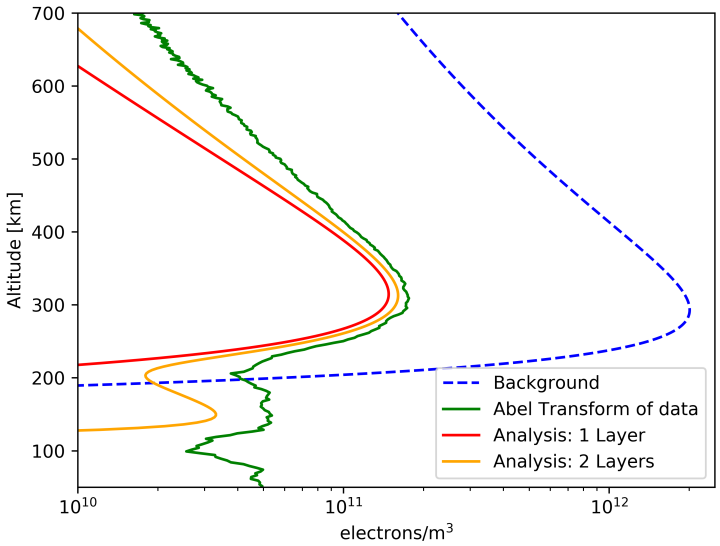

Figure 2.6: *A second example of the 1D-Var analysis.*

3 Model Developments

3.1 Additional Layers

The 1D-Var Vary-Chap model described in Section 2 has been written in FORTRAN. During this Visiting Scientist position the model has been written into Python and fully vectorized (a direct re-coding of the FORTRAN ran very slowly). Additionally the option of including additional layers has been included, for example one for each ionospheric layer (D, E, F1 and F2). An additional layer can be added to the topside of the ionosphere to account for the systematic underestimate of the Vary-Chap model above hmF2 [dSPTHP$^+$19]. The shape of various multi-layer Vary-Chap profiles using the parameters in Table 3.1 are shown in Figure 3.1.

Table 3.1: *Default Vary-Chap Parameters for up to 5-layers*

	Parameters			
	$NmF2$ (e$^-$/m^3)	$hmF2$ (km)	H_0 (km)	k
D-Region	2×10^8	70	5	0.05
E-Region	5×10^{10}	110	20	0.05
F1-Region	5×10^{11}	205	30	0.05
F2-Region	2×10^{12}	300	50	0.15
“Topside"	3×10^{11}	500	250	0.5

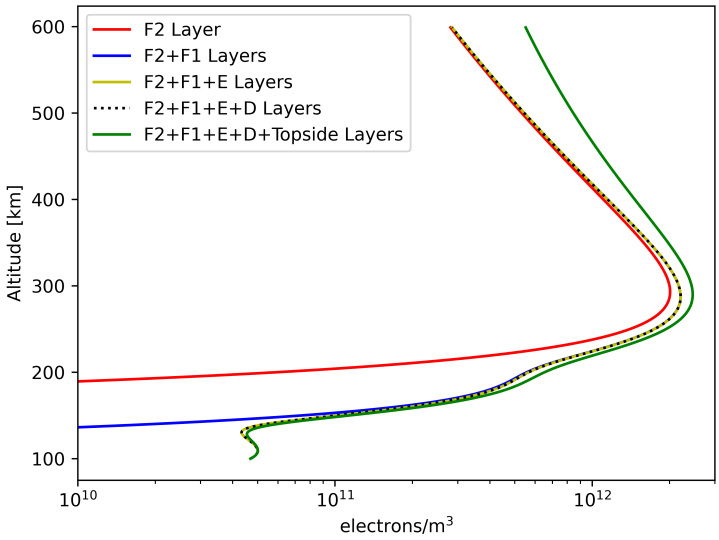

Figure 3.1: *Example of up to five layer Vary-Chap profiles with the parameters given in Table 3.1.*

The resulting five-layer Vary-Chap model provides an excellent approximation to the ionosphere, with a realistic looking E and F1 region. Using a fifth layer for the topside addresses the underestimation as highlighted by [dSPTHP$^+$19]. In practice the addition of the D-region layer has very little impact on the overall profile. Figure 3.2 shows the difference between the

five- and four-layer versions (excluding the D-region). The maximum difference is approximately 2×10^7, more than three orders of magnitude smaller than the D-region densities.

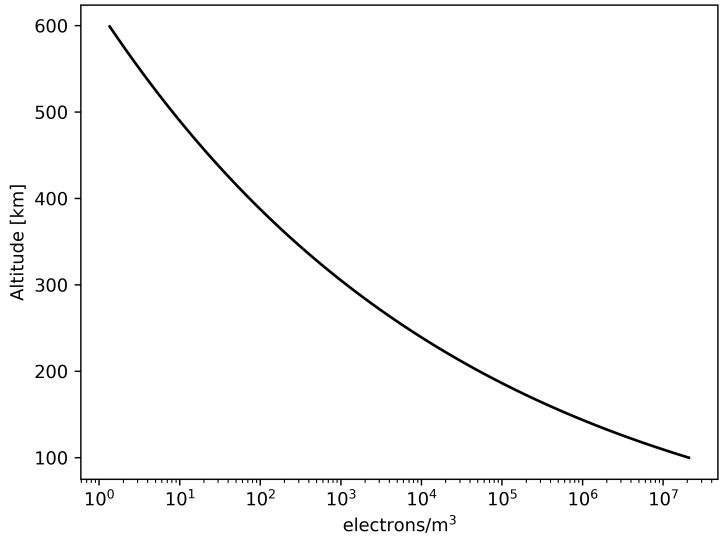

Figure 3.2: *Difference between including, or not, the D-Region layer in the Vary-Chap models.*

Whilst adding layers seemingly improves the overall shape of the ionosphere, this is done at a trade off of both computational time and number of iterations required for the 1D-Var to converge. These values are summarised in Table 3.2. Note that the maximum number of iterations was set to 50, and if this limit was reached then the process quit and it was recorded that the process failed to converge.

Table 3.2: *Average time per iteration, along with percentage of observations which converge and statistics of the rate of convergence for up to five Vary-Chap layers*

	Time per iteration (seconds)	Observations which converged	Iterations: Mean / Std. Dev.
1 layer	0.99	98.6%	16.2 7.1
2 layers	2.22	85.5%	34.1 8.0
3 layers	4.06	66.7%	28.1 9.1
4 layers	6.72	65.2%	28.7 9.1
5 layers	9.98	58.7%	30.7 11.4

It can be seen from Table 3.2 that the average time per iteration increases as the number of layers increase. However after an immediate jump in the average number of iterations when using one- and two-layer models, the average number of iterations for converging

observations remains fairly steady. This leads to a monotonic increase in the average total length of time needed for an observation to converge using the 1D-Var, Figure 3.3. However, the percentage of observations which converge continually decreases as the number of layers increases. From a high of 98.6% with just one-layer to only 58.7% with five-layers. This trade off must be considered when investigating the statistical performance when using a different number of layers in the analysis.

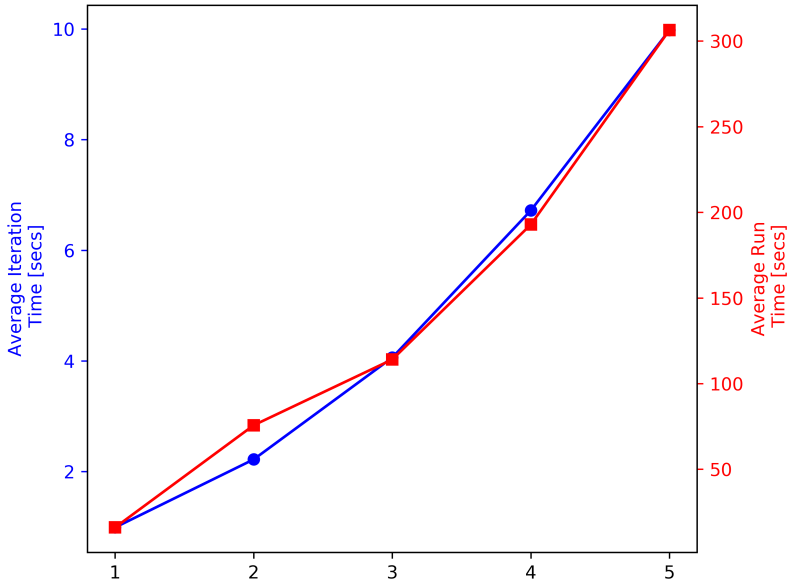

Figure 3.3: *Average time taken per iteration (blue) and total length of time for an observation to converge (red).*

3.2 Background Estimates

In this implementation of a 1D-Var system the background values which are used as an initial guess for the iteration process rather than an estimate for the analysis to be combined with the observations. For example, using further observational data from UPC, with a one-layer Vary-Chap and a variety of background parameters gives the analysis results, in the given number of iterations, shown in Table 3.3.

What is clear from Table 3.3 is that varying the background parameters has almost no impact on the final analysis (the only difference at all is in the third block with an $H_{0,F2}$ value of 49.9 where in all other instances it is 50.1). The main difference between varying the impact parameter is the difference on the number of iterations required to arrive at the analysis results. This varies from 14 iterations to 6. This suggests that an improved background guess will reduce the number of iterations required for the model to converge. The ROPP implementation uses the fixed values as given in Table 3.1.

Noting this increased performance from a more accurate background guess, a new model for these parameters is defined below.

Table 3.3: *Background and analysis parameters for a one-layer Vary-Chap with different background conditions.*

	Parameters				
	$NmF2$	$hmF2$	$H_{0,F2}$	k_{F2}	Number of iterations
Background	2.00×10^{12}	300	50.0	0.15	9
Analysis	5.66×10^{11}	244	50.1	0.14	
Background	7.00×10^{11}	300	50.0	0.15	11
Analysis	5.66×10^{11}	244	50.1	0.14	
Background	7.00×10^{11}	250	50.0	0.15	6
Analysis	5.66×10^{11}	244	49.9	0.14	
Background	2.00×10^{11}	300	50.0	0.15	14
Analysis	5.66×10^{11}	244	50.1	0.14	

3.2.1 NmF2 Model

NmF2, the peak density of the F2-layer, is dependent on a number of factors including geographical longitude (*lon*; in degrees), latitude (*lat*; degrees), time (UT; hours), season/day of year (DOY) and solar activity. A number of approaches can be used to described solar activity, for this simple model the sunspot number (SSN) is used. It is assumed that NmF2 varies independently with these parameters, an approach used by a number of empirical NmF2 models [JHM11, KCL$^+$09, KMW06]:

$$NmF2 = f_1(lon)f_2(lat)f_3(UT)f_4(DOY)f_5(SSN). \tag{3.1}$$

The five functions shown in Equation 3.1 are expanded below. The longitudinal component is best described by at least a four-order trigonometric function to account for the wave-4 longitudinal variation [HLWW11]. However since this model is only to be used to provide initial guesses a key requirement is ease and computational cheapness. To this end the longitude and latitude components are described by simple identities:

$$f_1(lon) = a_1 + \left(a_2\cos\left(a_3\frac{2\pi lon}{360}\right) + a_4\sin\left(a_5\frac{2\pi lon}{360}\right)\right) \tag{3.2}$$

$$f_2(lat) = b_1 + \left(b_2\cos\left(b_3\frac{2\pi lat}{180}\right) + b_4\sin\left(b_5\frac{2\pi lat}{180}\right)\right) \tag{3.3}$$

The universal time component is given as the sum of two trigonometric functions to capture the diurnal and semidiurnal variation [JHM11] also included a third term to account for the terdiurnal terms). Similarly the day of year is the sum of two trigonometric functions since the main seasonal components of electron density are annual and semi-annual:

$$f_3(UT) = c_1 + \sum_{i=1}^{2}\left[c_{2,i}\cos\left(c_{3,i}\frac{2\pi UT}{24}\right) + c_{4,i}\sin\left(c_{5,i}\frac{2\pi UT}{24}\right)\right] \tag{3.4}$$

$$f_4(DOY) = d_1 + \sum_{i=1}^{2}\left[d_{2,i}\cos\left(d_{3,i}\frac{2\pi DOY}{365.25}\right) + d_{4,i}\sin\left(d_{5,i}\frac{2\pi DOY}{365.25}\right)\right] \tag{3.5}$$

Finally, the measure of solar activity, sunspot number (available from [SIL21]), is described by a quadratic relationship (as is similarly done for F10.7 by e.g. [CL10])

$$f_5(SSN) = e_1 + e_2 SSN + e_3 SSN^2. \tag{3.6}$$

The resulting NmF2 model, Equation 3.1, is therefore a combination of 31 coefficients.

3.2.2 hmF2 Model

$hmF2$, the height of the F2 peak density, in the same way as $NmF2$ is dependent on the longitude, latitude, time, season and solar activity. As such the $hmF2$ model is described in exactly the same way as the $NmF2$ model in Section 3.2.1

$$hmF2 = g_1(lon)g_2(lat)g_3(UT)g_4(DOY)g_5(SSN). \tag{3.7}$$

Where

$$g_1(lon) = \alpha_1 + \left(\alpha_2\cos\left(\alpha_3\frac{2\pi lon}{360}\right) + \alpha_4\sin\left(\alpha_5\frac{2\pi lon}{360}\right)\right) \tag{3.8}$$

$$g_2(lat) = \beta_1 + \left(\beta_2\cos\left(\beta_3\frac{2\pi lat}{180}\right) + \beta_4\sin\left(\beta_5\frac{2\pi lat}{180}\right)\right) \tag{3.9}$$

$$g_3(UT) = \gamma_1 + \sum_{i=1}^{2}\left[\gamma_{2,i}\cos\left(\gamma_{3,i}\frac{2\pi UT}{24}\right) + \gamma_{4,i}\sin\left(\gamma_{5,i}\frac{2\pi UT}{24}\right)\right] \tag{3.10}$$

$$g_4(DOY) = \delta_1 + \sum_{i=1}^{2}\left[\delta_{2,i}\cos\left(\delta_{3,i}\frac{2\pi DOY}{365.25}\right) + \delta_{4,i}\sin\left(\delta_{5,i}\frac{2\pi DOY}{365.25}\right)\right] \tag{3.11}$$

$$g_5(SSN) = \varepsilon_1 + \varepsilon_2 SSN + \varepsilon_3 SSN^2. \tag{3.12}$$

The parameters $\alpha_j, \beta_j, \gamma_j, \delta_j, \varepsilon_j$ are coefficients determined during the fitting of this empirical model.

3.2.3 NmE Model

The peak density of the ionospheric E-region, NmE, is well modelled by a simple function based on the a seasonal relationship with F10.7 and solar zenith angle χ [LK97, NCR08]:

$$NmE = \frac{a_e}{80.616}\sqrt{F_{10.7}}\cos^{0.6}(\chi_{eff}) \tag{3.13}$$

where a_e is a seasonal term given by [NCR08] and χ_{eff} is the effective solar zenith angle given by

$$\chi_{eff} = \begin{cases} \chi, & \text{if } \chi \leq 86.23^o \\ 90 - 0.24e^{20-0.2\chi}, & \text{otherwise} \end{cases} \tag{3.14}$$

Where F10.7 in Equation 3.13 is the measure of the 10.7 cm flux from the Sun. It is related to the SSN as used in the previous sections by

$$SSN = \sqrt{167273 + (F_{10.7} - 63.7)1123.6} - 408.99. \tag{3.15}$$

3.2.4 hmE Model

Across a range of models including NeQuick ([NCR08]) and the Ionospheric Reference Model (IRI; e.g. [BR08]) hmE, the height of the E-region peak density, is usually set to a fixed height. In this model

$$hmE = 110 \text{ km} \tag{3.16}$$

as per the updated NeQuick model from [AEH18].

3.2.5 NmF1 Model

The critical density of the F1-layer, $NmF1$, is defined in this model, as in NeQuick [NCR08], in terms of the critical density of the E-Region. Specifically

$$NmF1 = 1.96NmE. \tag{3.17}$$

3.2.6 hmF1 Model

The height of the critical density of the F1-layer, $hmF1$, is also usually defined in terms of both $hmF2$ and hmE:

$$hmF1 = \frac{hmF2 + hmE}{2}. \tag{3.18}$$

3.3 Using the New Background Model

Table 3.3 demonstrated the impact of the background model values on the number of iterations needed to converge to a solution with the 1D-Var. Rather than using a fixed set of values for the initial guesses for the Vary-Chap layers but instead using values from the

model described in Section 3.2 has a major impact on the iteration rate and the total number of successful convergences, Table 3.4. The left-hand side of the table presents the same information as in Table 3.2 with the new values using the background model on the right-hand side.

Table 3.4: *Percentage of observations which converge and statistics of the rate of convergence for up to four Vary-Chap layers with different background conditions.*

	Background using Table 3.1		Background using model from Section 3.2	
	Observations which converged	Mean Iterations	Observations which converged	Mean Iterations
1 layer	98.6%	16	99.3%	11
2 layers	85.5%	34	92.7%	27
3 layers	66.7%	28	79.4%	25
4 layers	58.7%	31	72.8%	28

The four-layer Vary-Chap model in Table 3.4 is an E-, F1-, F2- and topside-layer model. The D-region is excluded as it has very little impact on the overall results (see Figure 3.2). It can be seen from Table 3.4 that using the new background model not only reduces the average number of iterations required for convergence in each case but also improves the overall percentage of observations which do converge. The average reduction in the number of observations is 4.5 iterations and the increased percentage of observation convergence means that all test versions of the model have at least a 70% convergence rate (improved from just 58.7%).

3.4 Observation Readers

The ROPP (Section 2) implementation of the 1D-Var code includes a reader for observational data from UPC (which has been written into Python during this project). During this project, additional code has been developed to read a wider set of datasets.

3.4.1 COSMIC-2

The FORMOSAT-7/COSMIC-2 constellation is a constellation of six identical satellites in a low inclination orbit at a nominal altitude of 520-550 km with an inclination of 24^o [AS19]. It follows the successful COSMIC-1 program, which launched in April 2006. The COSMIC-2 constellation's primary aim is to observe the atmosphere from an equatorial orbit using RO, supporting operational global weather prediction, tropical weather and climate research, space weather forecasting, and ionospheric research. Data from the COSMIC-2 mission is made available each day at 0200 UTC at https://data.cosmic.ucar.edu/gnss-ro/cosmic2/nrt/.

3.4.2 Spire Global

Spire Global currently operates a fleet of more than 110 CubeSats, the second largest commercial constellation by number of satellites, and the largest by number of sensors. The satellites are integrally designed and built by Spire themselves from Glasgow in the UK and its European headquarters in Luxembourg, with the capacity to build up to two satellites per

week. The satellites, designed for RO observations are 3U CubeSats which are three-axis stabilised. A day of example data files can be downloaded from the Spire website [UK"21], the TEC and associated signal-to-noise ratio (SNR) is shown in Figure 3.4.

The satellites are placed in low-Earth orbit (generally around 500 km so that they naturally de-orbit) at various inclinations, including equatorial, sun-synchronous and inclinations in between, which gives global coverage and the ability to listen to every spot on Earth more than 100 times per day. They are scheduled to be retired and replaced every two to three years.

The Spire's own global ground station network provides timely data that is processed by Spire to produce high-value information products and made available through their customer API.

An example of using Spire data in this 1D-Var system is shown in Figure 3.5. Figure 3.5a shows the $\partial STEC/\partial a$ observations, the background guess (in blue) and the analysis (in red) using a single, F2, layer. The resulting analysis provides an excellent match to the data, and shows a large change from the background estimate. Figure 3.5b shows the same results but in electron density space. Furthermore an Abel Transform of the data is over plotted (green) for comparison. The analysis closely agrees with the Abel Transform results up to the peak ($\sim$ 300 km) but then gives larger electron density values in the topside compared to the Abel.

3.4.3 NeQuick

NeQuick 2 is an ionospheric electron density model developed at the Aeronomy and Radiopropagation Laboratory (now Telecommunications/ICT for Development Laboratory) of the Abdus Salam International Centre for Theoretical Physics (ICTP), Trieste, Italy, and at the Institute for Geophysics, Astrophysics and Meteorology (IGAM) of the University of Graz, Austria [NCR08]. It is a climatological model of the ionosphere and the International Telecommunication Union Radiocommunication Sector (ITU-R) standard. It has been designed to have continuously integrable vertical profiles which allows for rapid calculation of the TEC for trans-ionospheric propagation applications. Between 100 km and the peak of the F2 layer, NeQuick uses an electron density profile based on five semi-Epstein layers [Eps30, Raw83] with modelled thickness parameters. Three profile anchor points are used: the E layer peak, the F1 peak (if present) and the F2 peak. The anchor points are defined in terms of the standard ionosonde parameters foE, foF1, foF2 and M(3000)F2 and the URSI coefficients are often used. A semi-Epstein layer represents the model topside with a height-dependent thickness parameter that has been empirically determined. NeQuick can be run up to a height of 25000 km, and is used in the Galileo GNSS system to calculate ionospheric corrections [AGG$^+$13].

For use in this 1D-Var system NeQuick has be used to generate simulated data. Both a 1D-version of NeQuick (where the electron density is constant in latitude and longitude) and a full 3D-version (as described in [AEH18]) have been used to create simulated results from realistic RO geometries (Figure 3.6). The resulting $\partial STEC/\partial a$ profiles are shown in Figure 3.7. Overall both the 1D and 3D give similar results, with most of the additional structure appearing in the 3D version below 100 km. This is explored further in Section 3.5.

3.4.4 AENeAS

The Advanced Ensemble electron density (Ne) Assimilation System (AENeAS; [EA19]) is a state-of-the-art physics-based data assimilation (DA) model of the upper atmosphere. AENeAS uses a localised ensemble transform Kalman filter (LETKF) to convolve ionospheric and thermospheric parameters, such as electron density, with modelled output from its background model, the Thermosphere Ionosphere Electrodynamics General Circulation Model (TIE-GCM) [QBE+14] and NeQuick [NCR08]. AENeAS has been shown to have excellent performance compared to independent observations [EA19, DE20].

Similarly to NeQuick-3D, AENeAS is a 3D model and so can only be used to simulate data through realistic RO geometries. Figure 3.8 shows observation data as well as the simulated data along the same ray paths from AENeAS and NeQuick-3D. From this it can be seen that AENeAS does a good job capturing the minima at ~ 300 km but both AENeAS and NeQuick underestimate the altitude of the peak (~ 100 km rather than ~ 180 km and overestimate its magnitude.

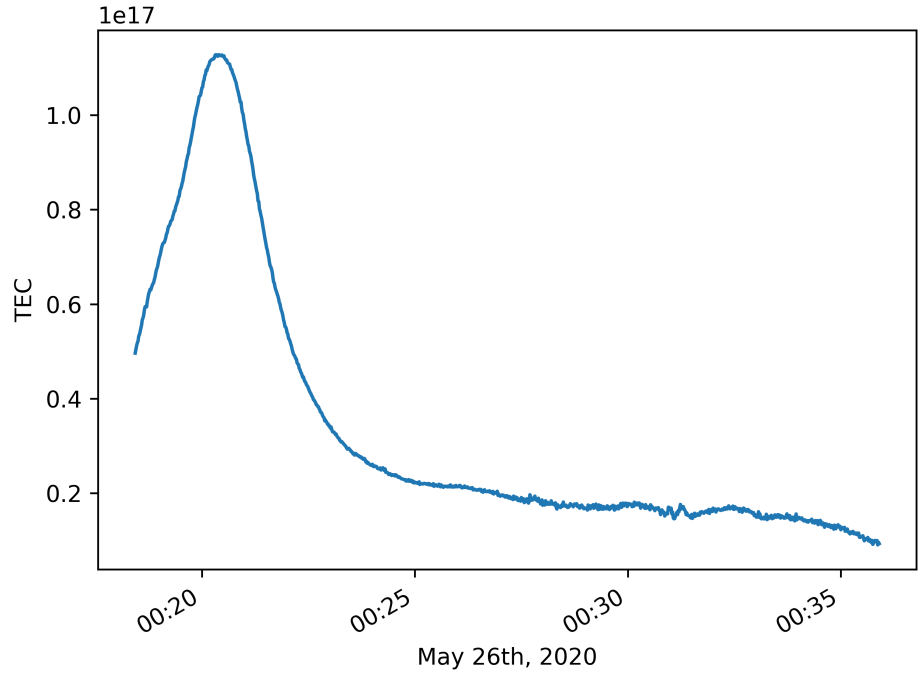

(a) Example Spire TEC observations

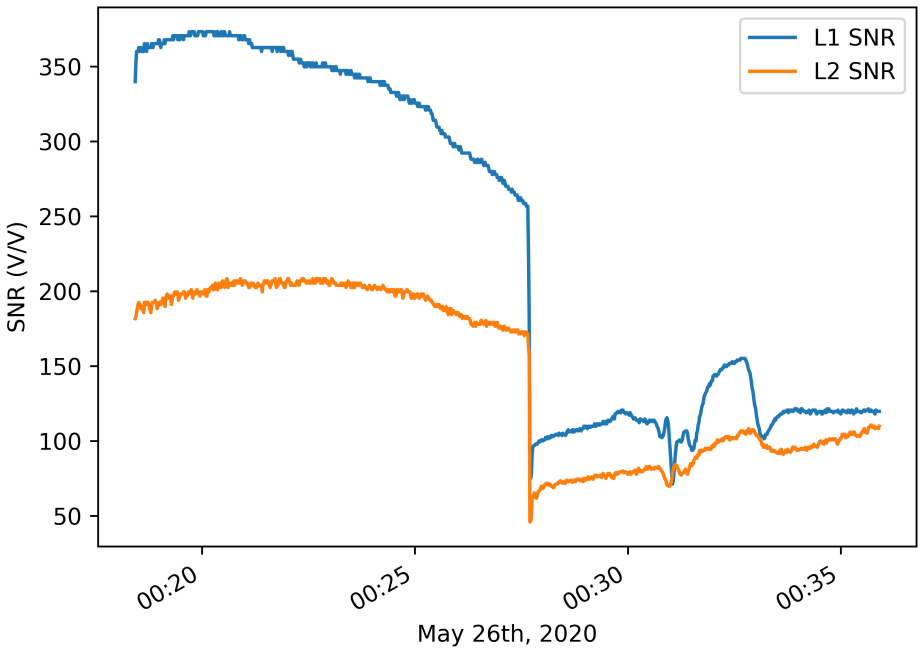

(b) Example Spire Signal-to-Noise Ratio

Figure 3.4: *Example Spire Data downloaded from Spire Website. Figure 3.4a shows the TEC observations and Figure 3.4b the associated Signal-to-Noise Ratio for L1 and L2.*

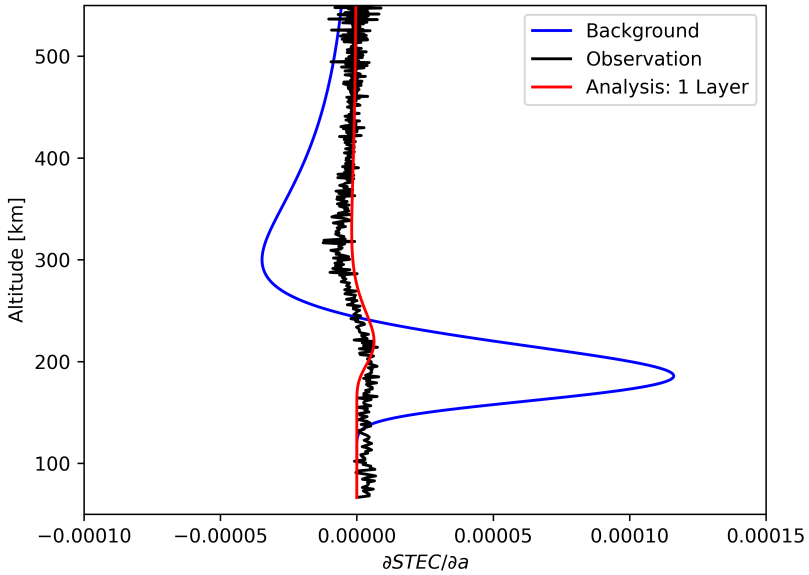

(a) *Results of using the example Spire data (Figure 3.4) with the 1D-Var system.*

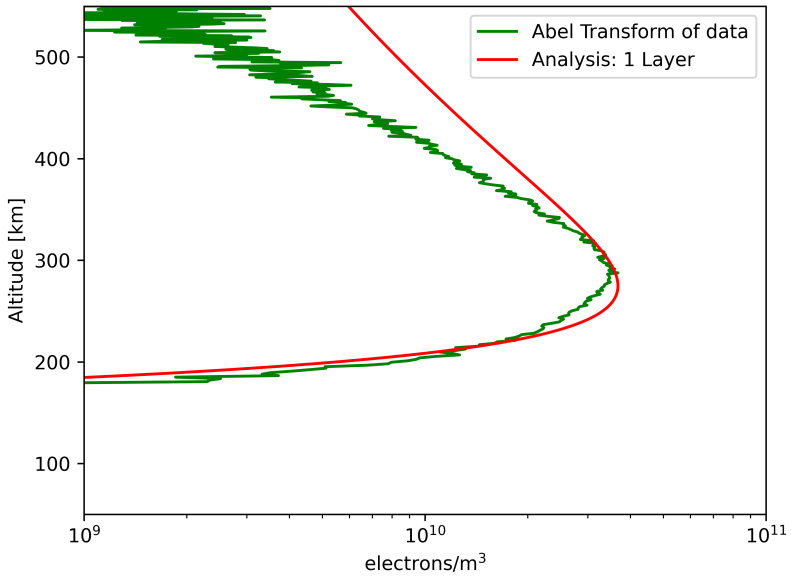

(b) *Same as 3.5a but in electron density space, with the Abel Transform of data shown for comparison.*

Figure 3.5

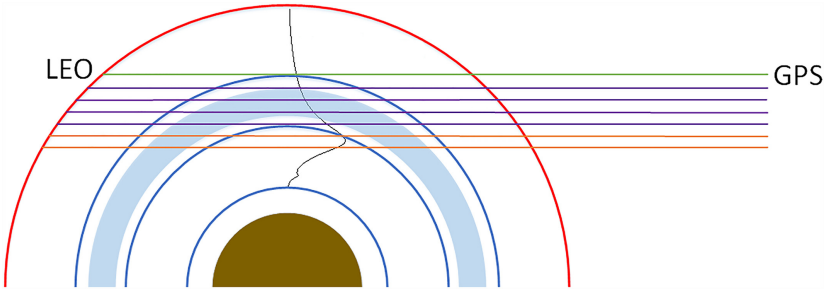

Figure 3.6: *Cartoon of how simulated RO geometries are created using NeQuick from Lyu et al. (2019)*

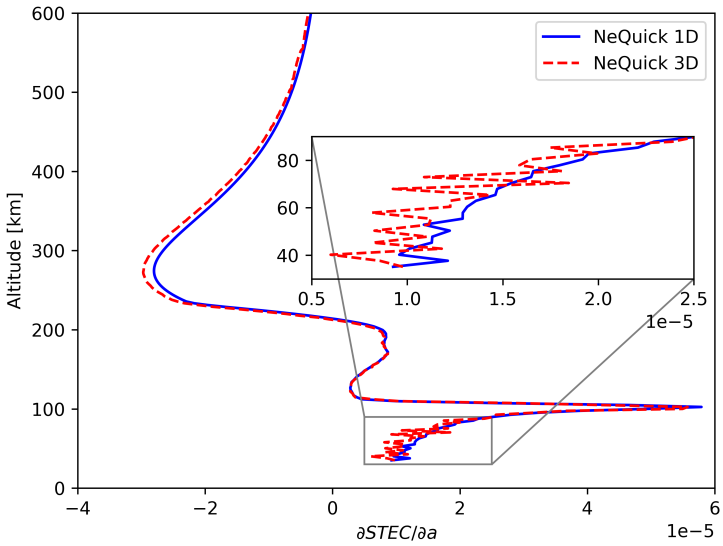

Figure 3.7: *Simulated data using a 1D and 3D version of NeQuick.*

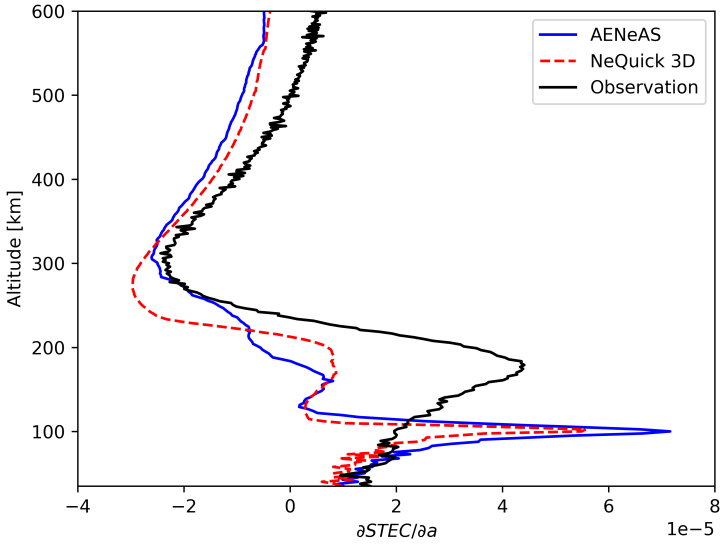

Figure 3.8: *Simulated data from AENeAS and NeQuick-3D, observational data for the same RO geometries is shown for comparison.*

3.5 Observation Uncertainty

In the ROPP implementation of this 1D-Var retrieval the observational error is set to a fixed error of 2 μrad for all altitudes. Accurate estimation of the uncertainty of the observations is crucial to ensure the observations are not over fitted. In general it is difficult to estimate the uncertainty of observations, since in most cases there is no additional, independent, reference truth.

In this work, as well as errors from the observations themselves, there are clearly errors generated from a 1D-retrieval compared to a full 3D-retrieval (e.g. Figure 3.7). These errors between a full 3D and simple 1D retrieval will depend on location, time of day and solar conditions. To estimate these errors RO geometries from 145 Metop-SG full occultations have been simulated through the 1D-NeQuick and 3D-NeQuick at four different solar activity levels: $F_{10.7} = 80, 30, 180, 230$. For each altitude the absolute mean error across all simulated occultations is then found, e.g.

$$\varepsilon(h) = \left| \frac{1}{580} \sum_{i=1}^{580} (N_i^{3D}(h) - N_i^{1D}(h)) \right| \tag{3.19}$$

where ε is the error, h a particular altitude, $N^{3D}(h)$ is the value of the 3D-NeQuick model at height h, $N^{1D}(h)$ the altitude of 1D-NeQuick and there are 580 values to average over since there are 145 RO geometries, each sampled through the ionosphere at four different activity levels. To ensure that "rare" geometries, such as occultations which cross through the day/night terminator, do not swamp the errors any outliers at each altitude are removed. Outliers are defined as any value which is less than 1.5 times the interquartile range (IQR) of the first quartile (Q1) of data or greater than 1.5 times the IQR of the third quartile (Q3), i.e. only data, d, in the range

$$Q1 - 1.5IQR \leq d \leq Q3 + 1.5IQR \tag{3.20}$$

is kept at each altitude.

The profile resulting from applying Equation 3.19 is shown in Figure 3.9. The red vertical line at 2 μrad is the default error used in ROPP. Figure 3.9 shows that 2 μrad is an excellent single value error to use (the overall average error is 2.04 μrad), however it is obvious the error is height dependent.

Rather than directly using the average errors from Figure 3.9 since they will be subject to sampling errors themselves a polynomial has been fitted to the data which can then be used in the 1D-Var. Figure 3.10 shows the residual sum of squares (RSS) error between a least-squares fitted polynomial of degree 2 to 16 compared to the data. The RSS error is defined as

$$RSS = \sum_{i=1}^{n} (x_i - f(x_i))^2 \tag{3.21}$$

where x_i is the ith variable to be predicted and $f(x_i)$ is the predicted value of x_i.

As expected, as the order of the polynomial increases the residual error decreases. The

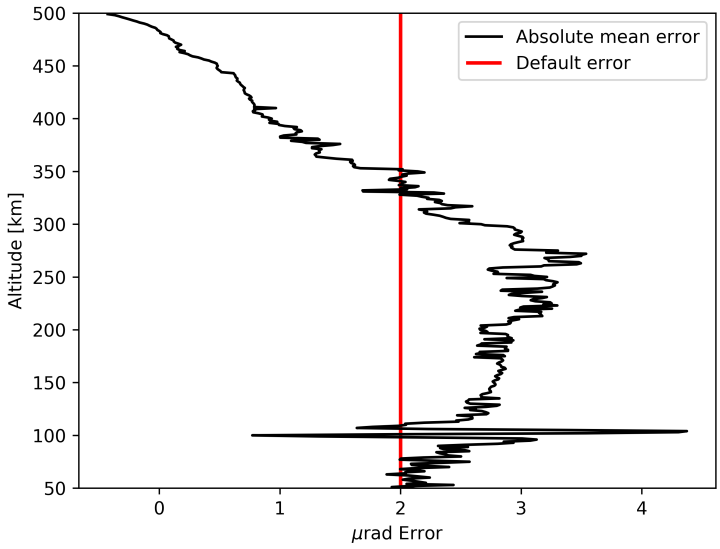

Figure 3.9: *Absolute mean error of RO geometries between using a 3D and 1D ionosphere.*

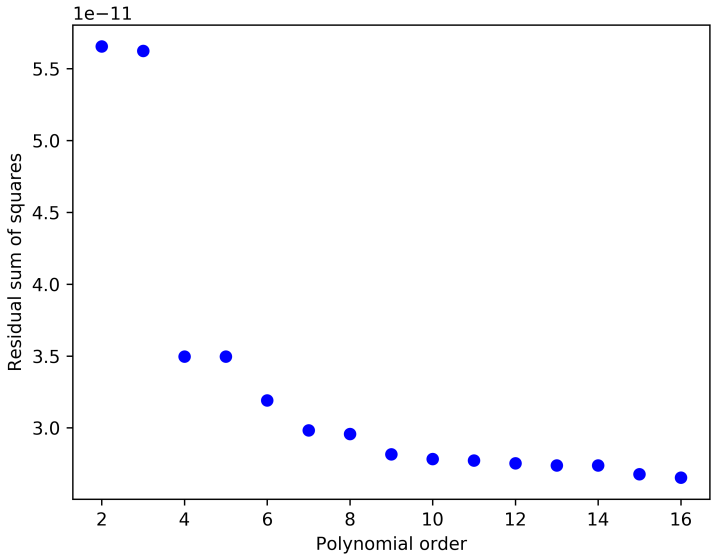

Figure 3.10: *Residual sum of squares error between order 2 to 16 polynomial fits and the data.*

biggest improvement in performance is between using an order 3 (cubic) polynomial and order 4. However noticeable improvements continue up until order 9 polynomials. Figure 3.11 shows the results of fitting an order 2 (quadratic) function (the simplest) and an order 9 polynomial to the data.

These polynomials are described by the expressions in Equation 3.22.

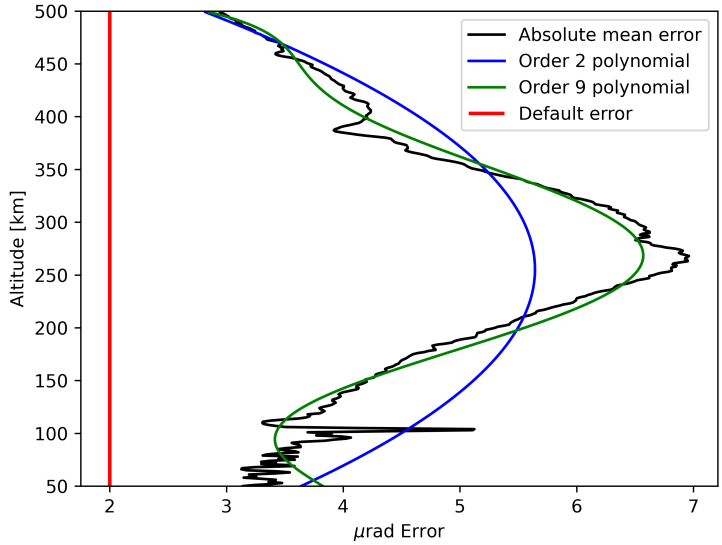

Figure 3.11: *Absolute mean error of RO geometries between using a 3D and 1D ionosphere with an order 2 and order 9 polynomial fitted to the data.*

$$x_2 = (-3.48\times10^{-11})y^2 + (1.26\times10^{-8})y + (1.78\times10^{-6})$$

$$\begin{aligned} x_9 = {} & (5.77\times10^{-27})y^9 - (1.26\times10^{-23})y^8 + (1.14\times10^{-20})y^7 \\ & - (5.51\times10^{-18})y^6 + (1.53\times10^{-15})y^5 - (2.46\times10^{-13})y^4 \\ & + (2.15\times10^{-11})y^3 - (8.53\times10^{-10})y^2 + (9.40\times10^{-9})y \\ & + (2.29\times10^{-6}) \end{aligned} \tag{3.22}$$

Example 1D-Var results using the three options for the observational errors are shown in Figure 3.12. It can be seen that each of the three different observation error models provide, at least slightly, different results. The fixed rate 2 μrad error and the order 2 polynomial error perform very similarly. The order 9 polynomial error profile provides a significantly different result, which is closer to the underlying observations. However use of the order 9 polynomial introduces significant risk to the numerical stability of the code and, as will be demonstrated in Section 4, only provides minimal improvement to the retrieval.

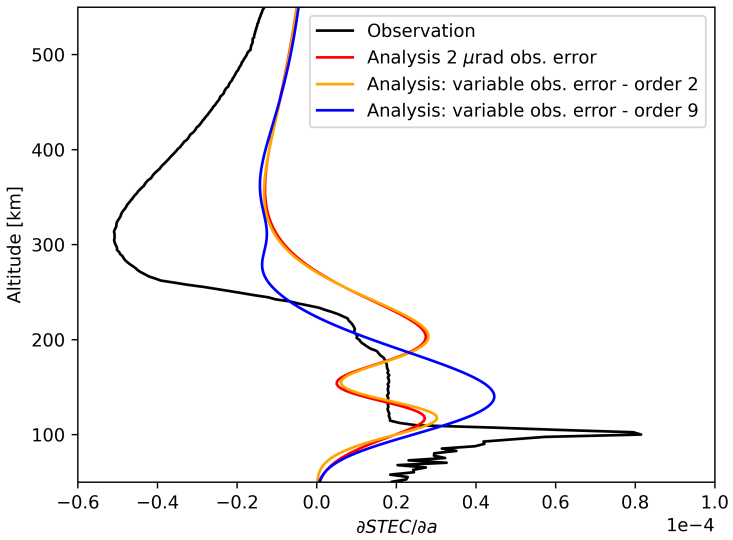

Figure 3.12: *Example 1D-Var analysis results using a fixed observation error, an order 2 polynomial fit and an order 9 polynomial fit error.*

4 Statistical Performance of the 1D-Var Retrieval

4.1 Introduction

To undertake a rigorous statistical analysis of the 1D-Var retrieval technique two things are needed:

1. a comparison to independent observations,
2. sufficient retrievals to reduce uncertainty in the analysis.

4.1.1 RO Observations

The current most abundant, and freely available, source of RO observations is from the COSMIC-2 satellites (see Section 3.4.1). To perform a rigorous statistical analysis of the 1D-Var retrieval technique all available Level 1B (TEC observations) and Level 2 (ionospheric profiles) products from 2020 have been used [COS19]. For COSMIC-2 the calibrated TEC data is derived from the L1 and L2 phase differences, which is then calibrated using the method described in CDAAC [SSS20].

In total there are 1,838,920 Level 1B occultations (each containing several hundred TEC observations) and an associated 966,358 Level 2 derived ionospheric profiles available to download in 2020.

4.1.2 Independent Observations

By stepping through a range of HF frequencies transmitted vertically upwards and measuring the return echoes ionosondes can image the vertical profile of the ionosphere up to the peak density. These observations are both widely assimilated by ionospheric models and also commonly used as reference observations (often incorrectly called 'truth') for comparative studies e.g. [FAJB$^+$11, EAN14, EAC$^+$17, STS11].

Ionosonde observations (profiles) from within 200 km of the location of the occultation have been used to validate both the COSMIC-2 profile reconstruction as well as the 1D-Var retrieval. [LLL$^+$20] and [CZB$^+$21] have previously validated the COSMIC-2 profiles, in terms of peak density/height, by comparison to ionosonde profiles at eight locations across one month in late 2019 and two months in early 2020 respectively. The [LLL$^+$20] study resulted in the comparison of 135 RO profiles and the [CZB$^+$21] study used ~2200 profiles. In this work every RO profile within 200 km of an ionosonde with available data is considered. This set of data is further reduced to try and account for errors in the reference observations. In general ionosonde profiles are autoscaled to get the true heights, but this can, and does, give rise to "autoscaling errors". The best way to overcome these errors is to manually scale the ionograms (as was done in [LLL$^+$20]), however that is a time consuming process. Another way to address the problem is by looking at the confidence scores that autoscaling software, such as ARITST [GKK$^+$08], uses to assess the success of the inversion. Here only profiles with maximum confidence (100) have been used. That results in 10,935 profiles. However, as can be seen in Figure 4.1, even profiles with the maximum confidence score can still contain errors. The profile in black in the figure is considered a 'sensible' profile whilst the others contain a variety of (potential) errors.

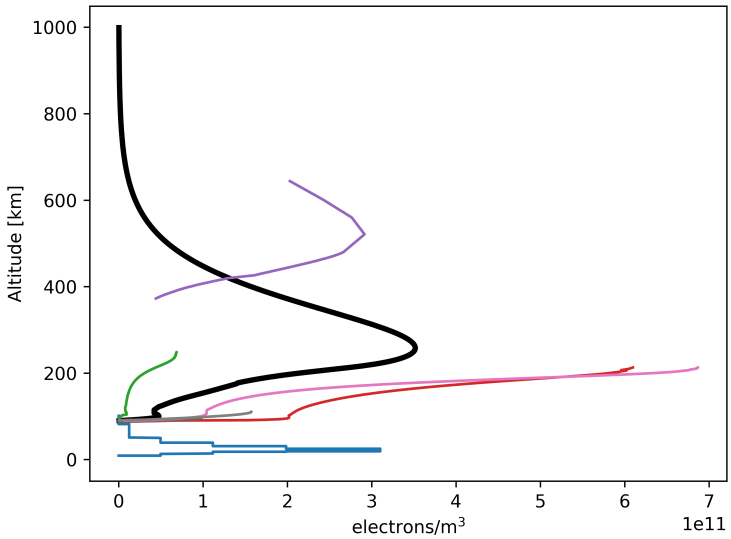

Figure 4.1: *Example electron density profiles from ionosonde observations which have been given the maximum confidence score from the autoscaling software. The profile in black is an example of a well inverted profile (and a maximum confidence score is expected). Non-black profiles provide evidence that a large confidence score does not result in an accurate inversion.*

To address this issue, each of the ionosonde profiles have been examined and removed from the analysis if they contain obvious errors. Overall this results in 10,612 profiles which are used in the analysis. The number of observations are summarized in Table 4.1.

Table 4.1: *Number of COSMIC-2 profiles analysed*

Total occultations	1,838,920	100.0%
Of which have associated profiles	966,358	52.5%
Of which have nearby ionosonde observations	10,935	0.59%
Of which do not contain obvious autoscaling errors	10,612	0.58%

4.2 Analysis Results

Initial analysis of the 1D-Var retrieval, in a similar approach to [LLL$^+$20], is to look at the performance of the F2 peak in terms of density and altitude compared to the ionosondes. These results can then be compared to the COSMIC-2 electron density profiles. However, before looking at the statistical performance of the two approaches, some quality control (QC) of the peak parameters is required.

An easy first approximation to find the F2 peak parameters is to take the maximum density of the electron density profile and associated altitude. The resulting probability density plots are shown in Figure 4.2: 4.2a the maximum density and 4.2b the associated altitudes of those densities. By comparing the COSMIC-2 height of maximums to the probability distribution function of hmF2's using data from the Chilton, UK ionosonde between 2000 and 2019,

Figure 4.3. It is clear that the main bulk of the distributions agree closely, however the second and third peaks centred at 100 km and just greater than 0 in the COSMIC-2 data are likely not actually hmF2 values. These likely included both observations of sporadic-E and other errors in the COSMIC-2 profiles (Figure 4.4). In this analysis hmF2 values are defined to be between 200 km and 500 km, if a value is outside of this range it is excluded from the analysis.

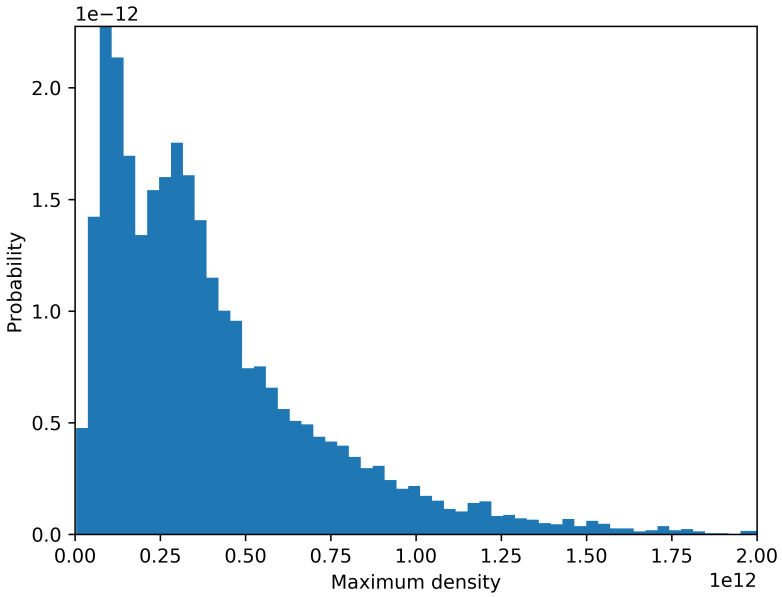

(a) COSMIC-2 maxmimum densities.

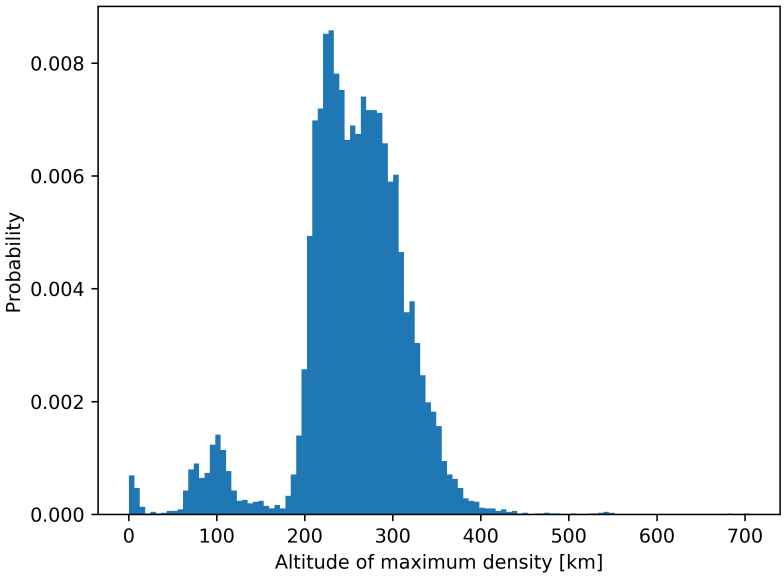

(b) COSMIC-2 height of maximum densities.

Figure 4.2: *Histograms of COSMIC-2 maxmimum densities and associated heights.*

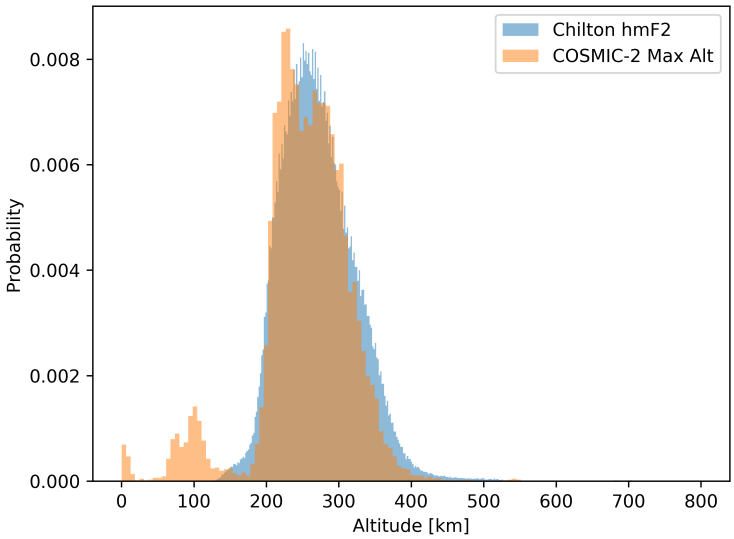

Figure 4.3: *Probability distribution function of COSMIC-2 maximum densities overlayed with hmF2 data from Chilton, UK ionosonde using data from 2000 to 2019.*

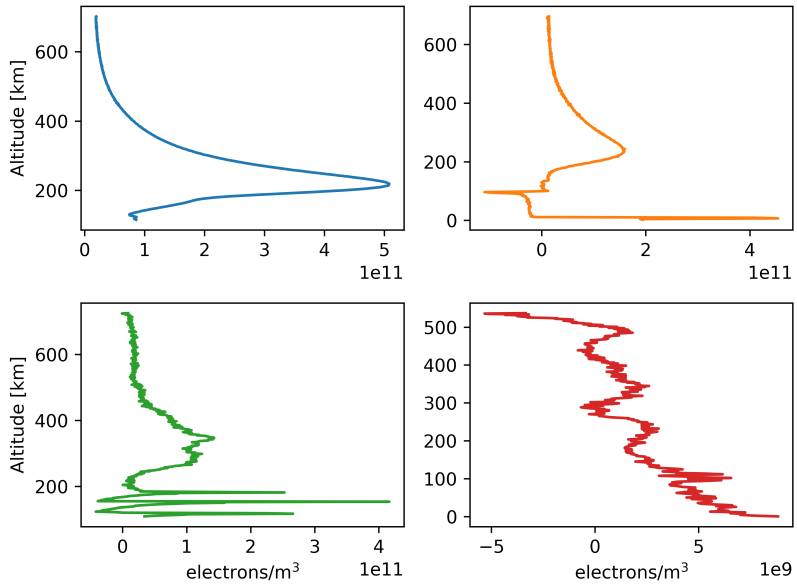

Figure 4.4: *Sample of COSMIC-2 electron density profiles.*

4.2.1 Statistical Performance

To provide a statistical comparison between the F2 peak parameters the relative percentage error ($\Delta X(\%) = 100(X - X_{ionosonde})/X_{ionosonde}$) of the specification of both NmF2 and hmF2 between these ionosonde observations with both the 1D-Var retrieval with up to four-layers and COSMIC-2 retrieval is shown in Table 4.2.

From these results you can see that the 1D-Var retrieval outperforms COSMIC-2 when using three or four layers. There is a 7% absolute error in the COSMIC-2 retrieval of NmF2 (which

Table 4.2: *Statistical performance of retrieving NmF2 and hmF2 from the 1D-Var compared with COSMIC-2*

	COSMIC-2	1D-Var			
		1 Layer	2 Layers	3 Layers	4 Layers
NmF2	7.0%	-14.8%	-10.6%	-5.3%	-4.2%
hmF2	2.6%	1.3%	0.7%	-0.1%	-0.1%

is consistent with the results of [CZB+21]) compared with -5.3% and -4.2% when using 1D-Var with three and four layers respectively. However, when only using one-layer the 1D-Var has a -14.8% error in the retrieval of the parameter. For hmF2 the COSMIC-2 error is 2.6% and all versions of the 1D-Var retrieval result in a smaller error decreasing from 1.3% to just -0.1%. However it should be noted that the autoscaled hmF2 errors can be large ($\sim \pm 10\%$) and this should be kept in mind when comparing the parameters.

A more detailed view of how the number of layers improves the F2 specification can be seen by looking at histograms of the data, Figure 4.5.

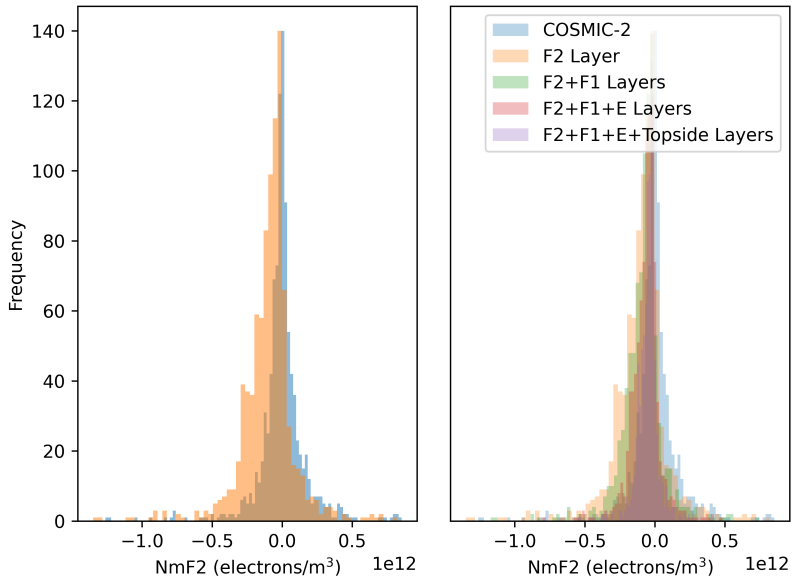

Figure 4.5: *Left hand plot shows histogram of COSMIC-2 and a one-layer 1D-Var retrieval errors for NmF2 compared to ionosonde observations. Right hand plot shows overlayed the results of the two, three and four-layer outputs.*

Whilst the individual, histograms on the right hand side of Figure 4.5 are quite difficult to differentiate between the overall trend of the reduction of mean and spread of the error with increasing number of layers is clear.

4.2.2 Bottomside Profile

Whilst the F2-peak is an important parameter and a good indicator of how well the 1D-Var retrieval is working, the reason behind using the Vary-Chap layers is to reconstruct the full ionospheric profile. To assess the bottomside performance all of the ionospheric profiles

(from the ionosonde, COSMIC-2 and the 1D-Var) are interpolated onto the same altitude grid, at 1 km resolution, and the root mean square error (RMSE) at each altitude is then calculated. The resulting RMSE altitude profile is shown in Figure 4.6.

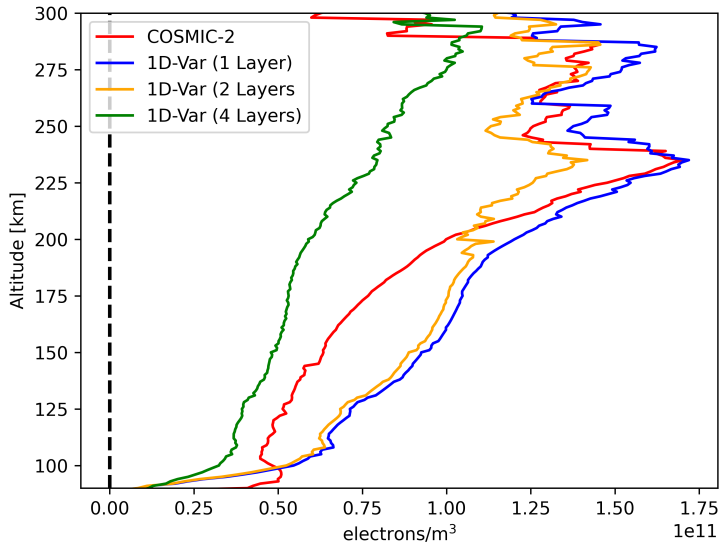

Figure 4.6: *Root mean square error (RMSE) altitude profiles for COSMIC-2 and the 1D-Var retrieval with only an F2 layer (blue), F2+F1 layers (orange) and F2+F1+E+Topside layers (green) compared to ionosonde observations.*

This shows that the 1D-Var retrieval with one-layer (F2) performs very similarly to the COSMIC-2 profiles throughout the bottomside. Above 225 km there is no statistically significant differences in the results. However when using two layers (F2+F1) this is an improvement in specification around the F2 peak (approximately 230 km). There is a small, almost constant offset, in improvement over the one-layer model below 200 km, but this is still significantly worse than the COSMIC retrieval. The four-layer (F2+F1+E+Topside) 1D-Var retrieval shows an excellent performance throughout the altitude range, with an improvement over COSMIC-2 by approximately 40%.

5 Conclusions and Recommendations

5.1 Conclusions

This visiting scientist project has taken the draft Radio Occultation Processing Package (ROPP) 11.0 FORTRAN code for a 1D-Var bending angle retrieval of the ionospheric profile using Vary-Chap functions, further developed it and statistically analysed the results. The new code has been written in Python, delivered to the ROM SAF, and the main model developments have been:

- Use of up to five Vary-Chap layers (D, E, F1, F2 and topside) for the retrieval
  - Quantify the increase run time for different number of layers,
  - Quantify the decrease in convergence rate.
- Develop a new, lightweight, peak parameter (NmF2, hmF2, NmF1, hmF1, NmE and hmE) model for the initialisation of the 1D-Var retrieval
  - Demonstrated an improvement in number of retrievals to successfully converge, and in the time taken to do so
- Enabled the use of new data RO data sources:
  - COSMIC-2,
  - Spire Global,
  - Simulated data through 3D-models (e.g. NeQuick and AENeAS).
- Developed two (2nd and 9th order) altitude varying uncertainty estimates for the assimilation.

With these model developments the 1D-Var retrieval has been compared with the COSMIC-2 profile retrieval using nearby ionosondes as independent observations. Using all available data from 2020 it has been shown that:

- The COSMIC-2 NmF2 has less error than the 1D-Var when using one or two Vary-Chap layers.
- The 1D-Var NmF2 is more accurate than the COSMIC-2 profiles when using three or four Vary-Chap layers.
- The 1D-Var provides a more accurate hmF2 for all layers.
- The root mean square error for the whole bottomside profile for a one-layer 1D-Var and COSMIC-2 is statistically similar.
- The root mean square error for the bottomside profile using a four-layer 1D-Var retrieval is significantly better than COSMIC-2's.

5.2 Recommendations

This work has provided evidence that the absolute ionospheric profile can be retrieved directly from the assimilation of bending angles, without the need for an estimate of differential code biases.

There are a number of subsequent research questions which should be investigated. In terms of further statistical analysis, further work on the model topside should be undertaken. The addition of a fourth topside layer has demonstrated improvement in specification of the whole bottomside of and the F2 peak density. The topside of the profile has not been investigated since the ionosonde observations rely heavily on their own mathematical models for that region. Instead other observations such as in-situ electron densities and/or incoherent scatter radar (ISR) observations could be use for independent validation of the approach, especially for the topside. Further model developments should also look to decrease the model run time when using four-layers and improve the criteria for success or failure when checking for convergence.

The usefulness of this approach should be demonstrated by using the ionospheric profile retrieval in an existing data assimilation scheme where traditionally DCBs have been required, such as the Advanced Ensemble electron density (Ne) Assimilation System (AENeAS) [EA19].

Acknowledgments

COSMIC-2 provisional space weather data are provided by COSMIC Data Analysis and Archive Center (https://doi.org/10.5065/t353-c093). The autoscaled ionograms were downloaded from NOAA's National enters for Environmental Information (http://ngdc.noaa.gov). Sample Spire Global data was downloaded from https://spire.com/earth-intelligence-data/. Thanks to Dr. Haixia Lyu and Dr. Hernández-Pajares for sample COSMIC-1 data and useful discussions during the project.

Crucially, thanks to Dr. Sean Healy and Dr. Ian Culverwell for continued and always insightful discussions throughout the work.

Bibliography

[AEH18] Matthew J Angling, Sean Elvidge, and Sean B. Healy. Improved model for correcting the ionospheric impact on bending angle in radio occultation measurements. *Atmospheric measurement techniques*, 11(4):2213–2224, April 2018.

[AGG+13] Antonio Angrisano, Salvatore Gaglione, Ciro Gioia, Marco Massaro, and Salvatore Troisi. Benefit of the NeQuick Galileo Version in GNSS Single-Point Positioning. *International Journal of Navigation and Observation*, 2013:1–11, 2013.

[AK06] Matthew J Angling and B. Khattatov. Comparative study of two assimilative models of the ionosphere. *Radio Science*, 41(5), 2006.

[Ang08] Matthew J Angling. First assimilations of COSMIC radio occultation data into the Electron Density Assimilative Model (EDAM). *Annales Geophysicae*, 26(2):353–359, 2008.

[AS19] R Anthes and W Schreiner. Six New Satellites Watch the Atmosphere over Earth's Equator. *Eos*, 100, 2019.

[BR08] D. Bilitza and B.W. Reinisch. International Reference Ionosphere 2007: Improvements and new parameters. *Advances in Space Research*, 42(4):599–609, August 2008.

[CL10] Yiding Chen and Libo Liu. Further study on the solar activity variation of daytime NmF2. *Journal of Geophysical Research: Space Physics*, 115(A12), 2010. _eprint: https://onlinelibrary.wiley.com/doi/pdf/10.1029/2010JA015847.

[COD21] CODE. Differential Code Biases (DCB), 2021.

[Con20] "ROM SAF Consortium". The Radio Occultation Proccessing Package (ROPP) Utilities Module User Guide. Technical report, September 2020.

[COS19] "UCAR/NCAR COSMIC". COSMIC-2 Data Products. 2019.

[Cul19] I D Culverwell. Sensitivity of some RO measurements to the shape of the ionospheric electron density profile. Technical Report ROM SAF Report 31, 2019.

[CZB+21] Iurii Cherniak, Irina Zakharenkova, John Braun, Qian Wu, Nicholas Pedatella, William Schreiner, Jan-Peter Weiss, and Douglas Hunt. Accuracy assessment of the quiet-time ionospheric F2 peak parameters as derived from COSMIC-2 multi-GNSS radio occultation measurements. *Journal of Space Weather and Space Climate*, 11:18, 2021. Publisher: EDP Sciences.

[DE20] Gareth Dorrian and Sean Elvidge. MIE5 Final Report. Part 2 – Model Testing. Technical Report SERENE/2020/003, University of Birmingham, UK, 2020.

[dSPTHP+19] Fabricio dos Santos Prol, David R. Themens, Manuel Hernández-Pajares, Paulo de Oliveira Camargo, and Marcio Tadeu de Assis Honorato Muella. Linear Vary-Chap Topside Electron Density Model with Topside Sounder and Radio-Occultation Data. *Surveys in Geophysics*, 40(2):277–293, March 2019.

[EA19] Sean Elvidge and Matthew J Angling. Using the local ensemble Transform Kalman Filter for upper atmospheric modelling. *Journal of Space Weather and Space Climate*, 9:A30, 2019.

[EAC+17] Sean Elvidge, Matthew J Angling, M Codrescu, M Fedrizzi, I A Galkin, M Hernandez-Pajares, N K Jackson-Booth, B Nava, A J Ridley, and D Roma-Dollase. A community wide ionospheric modelling challenge. In *XXXII URSI General Assembly and Scientific Symposium (URSI GASS)*, Montreal, Canada, 2017.

[EAN14] Sean Elvidge, Matthew J Angling, and Bruno Nava. On the use of modified Taylor diagrams to compare ionospheric assimilation models. *Radio Science*, 49(9):737–745, September 2014.

[Edd67] Amos Eddy. The Statistical Objective Analysis of Scalar Data Fields. *Journal of Applied Meteorology*, 6(4):597–609, 1967.

[Eps30] Paul S Epstein. Reflection of Waves in an Inhomogeneous Absorbing Medium. *Proceedings of the National Academy of Sciences*, 16(10), 1930.

[ESSD17] Eren Erdogan, Michael Schmidt, Florian Seitz, and Murat Durmaz. Near real-time estimation of ionosphere vertical total electron content from GNSS satellites using B-splines in a Kalman filter. *Annales Geophysicae*, 35(2):263–277, February 2017.

[Eve09] G Evensen. *Data Assimilation, the Ensemble Kalman Filter*. Springer-Verlag Berline Heidelberg, 2nd edition, 2009.

[FAJB+11] J. Feltens, Matthew J Angling, N. Jackson-Booth, N. Jakowski, M. Hoque, M. Hernández-Pajares, A. Aragón-Àngel, R. Orús, and R. Zandbergen. Comparative testing of four ionospheric models driven with GPS measurements. *Radio Science*, 46(6), December 2011.

[Gan63] L Gandin. *Objective analysis of meteorological fields (Leningrad: Gridromet). English translation (Jerusalem: Israel Program for Scientific Translation), 1965*. 1963.

[GKK+08] I Galkin, G Khmyrov, A Kozlov, B W Reinisch, X Huang, and V Paznukhov. The ARTIST 5. *Radio Sounding and Plasma Physics, AIP Proceedings #974*, 2008.

[HC15] S. B. Healy and I. D. Culverwell. A modification to the standard ionospheric correction method used in GPS radio occultation. *Atmospheric measurement techniques*, 8(8):3385–3393, August 2015.

[HLWW11] Maosheng He, Libo Liu, Weixing Wan, and Yong Wei. Strong evidence for couplings between the ionospheric wave-4 structure and atmospheric tides. *Geophysical Research Letters*, 38(14), 2011. _eprint: https://onlinelibrary.wiley.com/doi/pdf/10.1029/2011GL047855.

[JHM11] N. Jakowski, M. M. Hoque, and C. Mayer. A new global TEC model for estimating transionospheric radio wave propagation errors. *Journal of Geodesy*, 85(12):965–974, December 2011.

[Kal60] R E Kalman. A New Approach to Linear Filtering and Prediction Problems. *Transactions of the ASME-Journal of Basic Engineering*, 82:34–45, 1960.

[Kal03] E Kalnay. *Atmospheric Modeling, Data Assimilation and Predictability*. Cambridge University Press, Cambridge, 2003.

[KCL+09] Y. Kakinami, C. H. Chen, J. Y. Liu, K.-I. Oyama, W. H. Yang, and S. Abe. Empirical models of Total Electron Content based on functional fitting over Taiwan during geomagnetic quiet condition. *Annales Geophysicae*, 27(8):3321–3333, August 2009. Publisher: Copernicus GmbH.

[KMB+09] I. Kutiev, P. Marinov, A. Belehaki, B. Reinisch, and N. Jakowski. Reconstruction of topside density profile by using the topside sounder model profiler and digisonde data. *Advances in Space Research*, 43(11):1683–1687, June 2009.

[KMW06] Ivan S. Kutiev, Pencho G. Marinov, and Shigeto Watanabe. Model of topside ionosphere scale height based on topside sounder data. *Advances in Space Research*, 37(5):943–950, January 2006.

[LDT86] Francois-Xavier Le Dimet and Olivier Talagrand. Variational algorithms for analysis and assimilation of meteorological observations: theoretical aspects. *Tellus*, 38A:97–110, 1986.

[LHPMMC19] Haixia Lyu, Manuel Hernández-Pajares, Enric Monte-Moreno, and Estel Cardellach. Electron Density Retrieval From Truncated Radio Occultation GNSS Data. *Journal of Geophysical Research: Space Physics*, 124(6):4842–4851, 2019. _eprint: https://onlinelibrary.wiley.com/doi/pdf/10.1029/2019JA026744.

[LK97] R Leitinger and G Kirchengast. Easy to Use Global and Regional Ionospheric Models. A Report on Approaches Used in Graz. 32:329–342, 1997.

[LLL+20] Chi-Yen Lin, Charles Chien-Hung Lin, Jann-Yenq Liu, P. K. Rajesh, Tomoko Matsuo, Min-Yang Chou, Ho-Fang Tsai, and Wen-Hao Yeh. The Early Results and Validation of FORMOSAT-7/COSMIC-2 Space Weather Products: Global Ionospheric Specification and Ne-Aided Abel Electron Density Profile. *Journal of Geophysical Research: Space Physics*, 125(10):e2020JA028028, October 2020. Publisher: John Wiley & Sons, Ltd.

[NCR08] B Nava, P Coisson, and S Radicella. A new version of the neQuick ionosphere electron density model. *Journal of Atmospheric and Solar Terrestrial Physics*, 70(15):1856–1862, 2008.

[NRHB12] Patrick Nsumei, Bodo W. Reinisch, Xueqin Huang, and Dieter Bilitza. New Vary-Chap profile of the topside ionosphere electron density distribution for use with the IRI model and the GIRO real time data. *Radio Science*, 47(4), August 2012.

[Pla50] R L Plackett. Some theorems in least squares. *Biometrika*, 37(1-2):149–157, June 1950.

[QBE+14] Liying Qian, Alan G. Burns, Barbara A. Emery, Benjamin Foster, Gang Lu, Astrid Maute, Arthur D. Richmond, Raymond G. Roble, Stanley C. Solomon, and Wenbin Wang. The NCAR TIE-GCM: A Community Model of the Coupled Thermosphere/Ionosphere System. In Joseph Huba, Robert Schunk, and George Khazanov, editors, *Modeling the Ionosphere-Thermosphere System*, Geophysical Monograph Series, pages 73–83. John Wiley & Sons, Ltd, Chichester, UK, February 2014.

[Raw83] K Rawer. Replacement of the Present Sub-Peark Plasma Density Profile by a Unique Expression. *Advances in Space Research*, 2(10):183–190, 1983.

[RG69] H Rishbeth and O K Garriott. *Introduction to Ionospheric Physics*. Academic Press, London, 1969.

[RNHB07] B. W. Reinisch, P. Nsumei, X. Huang, and D. K. Bilitza. Modeling the F2 topside and plasmasphere for IRI using IMAGE/RPI and ISIS data. *Advances in Space Research*, 39(5):731–738, January 2007.

[Rod00] C D Rodgers. *Inverse methods for atmospheric sounding: theory and practice, Atmospheric, Oceanic and Planetary Physics*, volume 2. World Scientific Publishing, Singapore, 2000.

[SIL21] SILSO World Data Center. The International Sunspot Number (1868-2021). *International Sunspot Number Monthly Bulletin and online catalogue*, 2021. Place: Royal Observatory of Belgium, avenue Circulaire 3, 1180 Brussels, Belgium.

[SSRH99] W S Schreiner, S V Sokolovskii, C Rocken, and D C Hunt. Analysis and validation of GPS/MET radio occultation data in the ionosphere. *Radio Science*, 34(4):949–966, 1999.

[SSS20] Paul Strauss, William Schreiner, and Joseph Santiago. FORMOSAT-7/COSMIC-2 TGRS Space Weather Provisional Data Release 1. Technical report, 2020.

[STS11] L Scherliess, D C Thompson, and Robert W Schunk. Data assimilation models: A new tool for ionospheric science and applications. In W Liu and M Fujimoto, editors, *The Dynamics Magnetosphere*, pages 329–339. Springer, Berlin, 2011.

[Tal10] Olivier Talagrand. Variational Assimilation. In William Lahoz, Boris Khattatov, and Richard Menard, editors, *Data Assimilation: Making Sense of Observations*. Springer, 2010.

[UK"21] "Spire Global UK". Advanced Earth Intelligence Data, 2021.

[WHF21] Sicheng Wang, Sixun Huang, and Hanxian Fang. A Novel Method for Deriving the Vary-Chap Scale Height Profile in the Topside Ionosphere. *Journal of Geophysical Research: Space Physics*, 126(2), 2021. _eprint: https://onlinelibrary.wiley.com/doi/pdf/10.1029/2020JA028514.